Pergamon

Int. J. Solids Structures Vol. 32, No. 17/18, pp. 2571–2590, 1995

0020-7683/95 $9.50 + .00

0020-7683(94)00283-5

ANALYSIS OF A BRITTLE–DUCTILE TRANSITION UNDER DYNAMIC SHEAR LOADING

A. NEEDLEMAN
Division of Engineering, Brown University, Providence, RI 02912, U.S.A.

and

V. TVERGAARD
Department of Solid Mechanics, The Technical University of Denmark, Lyngby, Denmark

(*Received* 3 *February* 1994)

Abstract—The competition between brittle and ductile modes of failure is analyzed in a double edge-cracked specimen impacted by a projectile on the cracked side. Full transient analyses under plane strain conditions are carried out, with impact simulated by an imposed normal velocity with a small rise time. The material response is characterized by an elastic–viscoplastic constitutive relation for a porous plastic solid, with adiabatic heating due to plastic dissipation and the resulting thermal softening accounted for. The onset of cleavage is assumed to occur when a critical value of the maximum principal stress is attained. Effects of varying the loading rate and the thermal softening characterization of the material are explored. If the thermal softening rate is sufficiently high, a transition from a brittle failure mode at low loading rates to a ductile failure mode at high loading rates is found, which is quite the opposite of the usual brittle–ductile transition behavior. This prediction for the fracture mode transition is consistent with experimental observations under these loading conditions. Additionally, the failure paths indicated by the calculations are consistent with what is seen in experiments. The mechanism precipitating the brittle–ductile transition is a greater increase in peak strain magnitude than in peak stress magnitude with increased loading rate. When the strains ahead of the crack tip become large enough, thermal softening and possibly porosity-induced softening can lead to a localization of deformation, which limits the peak value of the maximum principal stress so that cleavage does not occur and the failure mode is ductile.

1. INTRODUCTION

A numerical procedure for the analysis of dynamic crack growth in elastic–plastic solids has been developed by Needleman and Tvergaard (1991a,b) based on the failure predictions of a porous plastic material model that represents ductile fracture by the nucleation and subsequent growth of voids to coalescence. In this procedure the computed crack growth paths and speeds rely entirely on the failure predictions of the material model. The material model used is elastic–viscoplastic with a temperature-dependent flow strength, and thermal softening due to adiabatic heating is accounted for. Recently, the computational method has been extended also to account for crack growth by cleavage fracture, in order to study the brittle–ductile transition (Tvergaard and Needleman, 1993). The method has been used to analyze a double edge-cracked specimen under axial loading (Needleman and Tvergaad, 1991a,b), or a single edge-cracked specimen that models experiments of Prakash and Clifton (1992), Tvergaard and Needleman (1992, 1993). For both specimens crack growth occurs under pure mode I or nearly pure mode I conditions.

A length scale has been introduced into the elastic–viscoplastic porous ductile material model by representing two populations of second phase particles; large inclusions with low strength, which result in large voids near the crack tip at an early stage, and small particles, which require large strains before cavities nucleate. For the larger voids the size and spacing are explicitly specified, whereas no length scale is specified for the small scale voids. The mesh-sensitivity of the dynamic crack growth predictions has been studied by Needleman and Tvergaard (1994). Cases where the large scale voids dominate show practically no mesh sensitivity, while a clear mesh sensitivity is found for cases dominated by the small scale voids. The initiation of crack growth is quite sensitive to the mesh for initially sharp cracks, whereas this sensitivity is removed for initially blunt cracks.

An experimental technique for subjecting edge cracks in plate specimens to high rates of shear loading (near mode II conditions) has been proposed by Kalthoff and Winkler (1988) and Kalthoff (1988). The method relies on impacting a plate by a cylindrical projectile between two parallel edge cracks. In experiments on a high-strength steel it was observed that at low impact velocities a brittle cleavage fracture occurred, whereas at sufficiently high impact velocities the failure involved shear localization leading to ductile fracture. The same fracture mode transition has been observed by Ravi-Chandar (1994) in polycarbonate using a loading arrangement like that described by Kalthoff (1988), but with a single edge-cracked specimen. Experiments with the single edge-cracked specimen focusing on shear band propagation in a high-strength steel are described by Mason *et al.* (1994). The fracture mode transition observed by Kalthoff and Winkler (1988) and Ravi-Chandar (1994) is, of course, the opposite of the usual brittle–ductile transition behavior.

An elastic analysis of wave propagation in the Kalthoff (1988) specimen has been carried out by Lee and Freund (1990), to study the combination of transient mode I and mode II deformation fields near the initial crack tip. The predicted time development of the mode II stress intensity factor was in reasonable agreement with the shadow optical measurements of Kalthoff (1988). In addition, the development of a compressive mode I stress intensity factor was predicted. Finite element analyses of the evolution of the ductile failure mode were reported by Zhou *et al.* (1994).

In the present paper, the competition between the brittle and ductile modes of failure in the Kalthoff (1988) specimen is analyzed using the elastic–viscoplastic porous material model with thermal softening, and incorporating a simple cleavage fracture criterion. Both low and high impact velocities are considered, and the predictions for initial failure are compared with experimental observations.

2. PROBLEM FORMULATION AND SOLUTION PROCEDURE

Here, as in previous studies [e.g. Needleman and Tvergaard (1991a,b); Tvergaard and Needleman (1993)], a convected coordinate Lagrangian formulation is used with the dynamic principle of virtual work written as

$$\int_V \tau^{ij}\delta E_{ij}\,\mathrm{d}V = \int_S T^i\delta u_i\,\mathrm{d}S - \int_V \rho\frac{\partial^2 u^i}{\partial t^2}\delta u_i\,\mathrm{d}V \tag{1}$$

with

$$T^i = (\tau^{ij}+\tau^{kj}u^i_{,k})v_j \tag{2}$$

$$E_{ij} = \tfrac{1}{2}(u_{i,j}+u_{j,i}+u^k_{,i}u_{k,j}), \tag{3}$$

where τ^{ij} are the contravariant components of Kirchhoff stress on the deformed convected coordinate net, v_j and u_j are the covariant components of the reference surface normal and displacement vectors, respectively, ρ is the mass density, V and S are the volume and surface of the body in the reference configuration, and $(\,)_{,i}$ denotes covariant differentiation in the reference frame.

The computations are carried out for the configuration shown in Fig. 1. This is a two-dimensional plane strain model of the specimen developed by Kalthoff (1988). A Cartesian coordinate system is used as reference, with the y^1–y^2 plane being the plane of deformation. The specimen dimensions are taken as $2L = 0.2$ m and $b = 0.1$ m, the initial crack length is $a = 0.05$ m, and the distance between the two cracks is $2h = 0.05$ m. The crack is taken to have a semi-circular tip, with initial opening, $\delta_t = 70$ μm [as indicated on the mesh plot of Fig. 3(b)]. Symmetry about the y^1-axis is assumed, so that the boundary conditions on the region analyzed numerically are

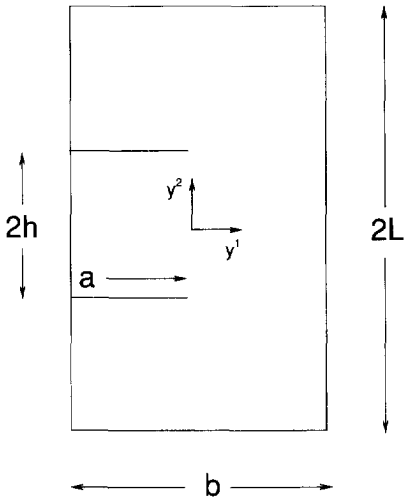

Fig. 1. Geometry of the shear loaded cracked specimen.

$$T^1 = 0, \quad u^2 = 0 \quad \text{on} \quad y^2 = 0 \tag{4}$$

$$u_1 = \int V(t)\,\mathrm{d}t, \quad T^2 = 0 \quad \text{on} \quad y^1 = -a \quad \text{and} \quad 0 \leqslant y^2 \leqslant (h-\delta_t/2), \tag{5}$$

where $V(t)$ is given by

$$V(t) = \begin{cases} V_1 t/t_r, & \text{for } t \leqslant t_r; \\ V_1, & \text{for } t_r < t. \end{cases} \tag{6}$$

and

$$T^1 = 0, \quad T^2 = 0 \tag{7}$$

on all remaining surfaces including the crack surface.

In the experiments reported in Kalthoff (1988) and Kalthoff and Winkler (1988), a projectile is accelerated to velocities of from 10 to 100 m s^{-1} and impacts the specimen between the two cracks. Assuming that material near the impact surface remains elastic and that the projectile and specimen have the same elastic properties, the impact conditions are replaced by the imposed velocity condition (6) with V_1 taken to be half the projectile velocity (as given by elastic wave theory). For numerical convenience, an initial rise time t_r is specified, which in the calculations here is fixed at 1.0 μs.

The total rate of deformation, $\mathbf{d}$ (the symmetric part of $\dot{\mathbf{F}} \cdot \mathbf{F}^{-1}$, where $\mathbf{F}$ is the deformation gradient), is written as the sum of an elastic part, $\mathbf{d}^e$, a viscoplastic part, $\mathbf{d}^p$, and a part due to thermal straining, $\mathbf{d}^T$,

$$\mathbf{d} = \mathbf{d}^e + \mathbf{d}^p + \mathbf{d}^T \tag{8}$$

with

$$\mathbf{d}^e = \mathscr{L}^{-1} : \hat{\boldsymbol{\sigma}}, \quad \mathbf{d}^T = \alpha \dot{T} \mathbf{1}, \tag{9}$$

where $\hat{\boldsymbol{\sigma}}$ is the Jaumann rate of Cauchy stress, α is the thermal expansion coefficient, $\mathbf{A} : \mathbf{B} = A^{ij} B_{ij}$ and

$$\mathscr{L} = \frac{E}{1+\nu}\left[\mathbf{I}' + \frac{\nu}{1-2\nu}\mathbf{I}\otimes\mathbf{I}\right]. \tag{10}$$

In eqn (10), E is Young's modulus, ν is Poisson's ratio, $\mathbf{I}$ and $\mathbf{I}'$ are the second and fourth order identity tensors, respectively, and $\otimes$ is the tensor product, $(\mathbf{A}\otimes\mathbf{B})^{ijkl} = A^{ij}B^{kl}$.

The basis for the plastic flow rule is a flow potential Φ, introduced by Gurson (1975), that characterizes the porosity in terms of a single scalar internal variable, f, the void volume fraction,

$$\Phi = \frac{\sigma_e^2}{\bar{\sigma}^2} + 2q_1 f\cosh\left(\frac{3q_2\sigma_h}{2\bar{\sigma}}\right) - 1 - q_1^2 f^2 = 0, \tag{11}$$

where $\bar{\sigma}$ is the average flow strength of the matrix,

$$\sigma_e^2 = \tfrac{3}{2}\boldsymbol{\sigma}':\boldsymbol{\sigma}', \quad \boldsymbol{\sigma}' = \boldsymbol{\sigma} - \sigma_h\mathbf{I}, \quad \sigma_h = \tfrac{1}{3}\boldsymbol{\sigma}:\mathbf{I} \tag{12}$$

and q_1 and q_2 are the parameters introduced by Tvergaard (1981, 1982). The porous plastic constitutive relation used in the calculations actually incorporates a modification due to Tvergaard and Needleman (1984) that models the effect of rapid coalescence at failure. However, this modification does not become active in the analyses here.

The viscoplastic part of the rate of deformation, $\mathbf{d}^p$, is taken in a direction normal to the flow potential and the constant of proportionality is determined by setting the aggregate plastic work rate equal to the matrix dissipation giving,

$$\mathbf{d}^p = \left[\frac{(1-f)\bar{\sigma}\dot{\bar{\varepsilon}}}{\boldsymbol{\sigma}:(\partial\Phi/\partial\boldsymbol{\sigma})}\right]\frac{\partial\Phi}{\partial\boldsymbol{\sigma}}. \tag{13}$$

The rate of increase of the void volume fraction results from the growth of existing voids and from the nucleation of new voids, which is taken to be strain controlled so that

$$\dot{f} = (1-f)\mathbf{d}^p:\mathbf{I} + \mathscr{D}\dot{\bar{\varepsilon}}. \tag{14}$$

Initially, the void volume fraction is zero and void nucleation is taken to follow a normal distribution (Chu and Needleman, 1980),

$$\mathscr{D} = \frac{f_N}{s_N\sqrt{(2\pi)}}\exp\left[-\frac{1}{2}\left(\frac{\bar{\varepsilon}-\varepsilon_N}{s_N}\right)^2\right] \tag{15}$$

with $\varepsilon_N = 0.15$, $f_N = 0.02$ and $s_N = 0.1$.

The matrix plastic strain rate, $\dot{\bar{\varepsilon}}$, is given by

$$\dot{\bar{\varepsilon}} = \dot{\varepsilon}\left(\frac{\bar{\sigma}}{g(\bar{\varepsilon},T)}\right)^{1/m}, \quad g(\bar{\varepsilon},T) = \sigma_0[1-\beta(T-T_0)][1+\bar{\varepsilon}/\varepsilon_0]^N, \tag{16}$$

where T is the temperature and $\bar{\varepsilon} = \int\dot{\bar{\varepsilon}}\,dt$.

Adiabatic conditions are assumed and the balance of energy gives

$$\rho c_p\frac{\partial T}{\partial t} = \chi\boldsymbol{\tau}:\mathbf{d}^p. \tag{17}$$

Here, ρ is the density in the reference configuration, c_p is the heat capacity, and the

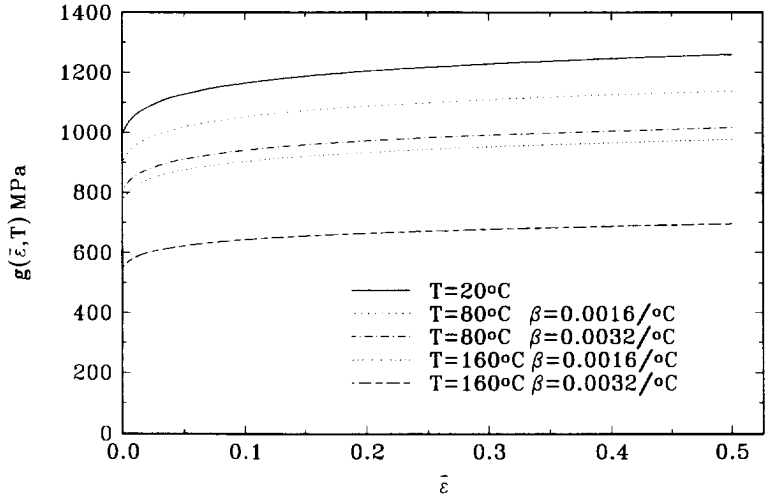

Fig. 2. Matrix hardness as a function of plastic strain at various temperatures for two values of the thermal softening parameter β.

parameter χ specifies the fraction of plastic stress work converted to heat, which is taken to have the value 0.90 (Taylor and Quinney, 1934).

The material parameters are taken to have values representative of a high-strength steel; $E = 202$ GPa, $\nu = 0.3$, $\sigma_0 = 1000$ MPa, $N = 0.05$, $m = 0.01$ and $\rho = 7600$ kg $m^{-3} = 7.6 \times 10^{-3}$ MPa m^{-2} s^2. The reference temperature T_0 is taken as 20°C, $c_p = 465$ J kg^{-1} $°C^{-1}$, $\alpha = 1 \times 10^{-5}$ $°C^{-1}$, and calculations are carried out using both $\beta = 0.0016°C^{-1}$ and $\beta = 0.0032$ $°C^{-1}$. Figure 2 shows the matrix hardness g as a function of plastic strain at various temperatures for these two values of β.

Ritchie *et al.* (1973) proposed a cleavage criterion based on a critical stress over a critical distance. Other models have been developed using a weakest link theory and Weibull statistics to develop expressions for the probability of cleavage in front of a crack tip (Mudry, 1987). Tvergaard and Needleman (1993) used a model based on partitioning the material into cleavage grains and assuming that cleavage failure in a grain occurs when the volume average of the maximum principal stress over that grain reaches a critical value. Recent calculations of Finot *et al.* (1994) for crack initiation and growth in the ceramic reinforcement in metal–matrix composite materials indicate that this is a reasonable approximation. In the present calculations, attention is confined to the very early stages of cleavage crack growth and the onset of cleavage is simply modeled by assuming that cleavage failure begins when the maximum principal stress reaches a temperature independent critical value, σ_c, which is taken to be constant throughout the specimen.

The generalization of Rice's (1968) J integral for dynamic loading conditions can be expressed as (Moran and Shih, 1987a,b)

$$J = \int_\Gamma \left[(W+L)\,\mathrm{d}y^2 - T^i u_{i,1}\,\mathrm{d}s \right] + \int_A \left[\alpha \tau_k^k T_{,1} + \rho \frac{\partial^2 u^i}{\partial t^2} u_{i,1} - \rho \frac{\partial u^i}{\partial t}\left(\frac{\partial u_i}{\partial t}\right)_{,1} \right] \mathrm{d}A, \qquad (18)$$

where A is the area inside the contour Γ.

The mesh used for the computations is shown in Fig. 3, where each quadrilateral consists of four "crossed triangle" linear displacement finite elements. The equations resulting from substituting the finite element discretization into eqn (1) are of the form

$$\mathbf{M}\frac{\partial^2 \mathbf{U}}{\partial t^2} = \mathbf{R}, \qquad (19)$$

where $\mathbf{M}$ is a mass matrix, $\mathbf{U}$ is the nodal displacement vector and $\mathbf{R}$ is the nodal force vector. The equations of motion (19) are integrated numerically by an explicit integration

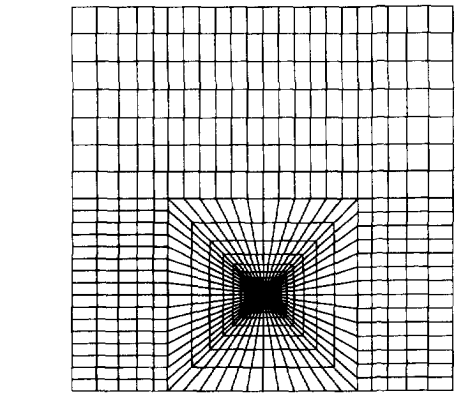

(a)

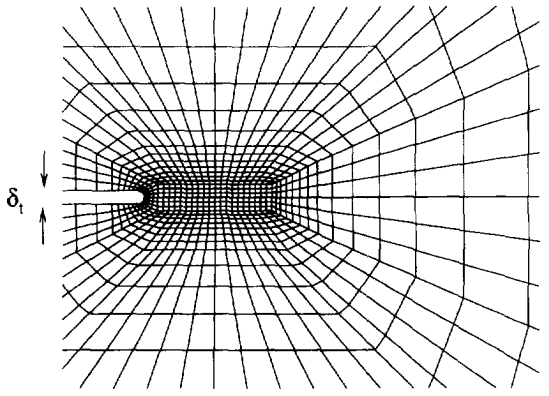

(b)

Fig. 3. Finite element mesh. Each quadrilateral consists of four "crossed" triangles. (a) Quadrant analyzed numerically. (b) Inner mesh showing the location of the initial crack tip. In presenting the numerical results, attention will focus on distributions of field quantities in this region.

procedure, the Newmark β-method with $\beta = 0$ (Belytschko *et al.*, 1976). A lumped mass matrix is used instead of the consistent mass matrix, since this has been found to be preferable for explicit time integration procedures, from the point of view of accuracy as well as computational efficiency (Krieg and Key, 1973). The constitutive updating is based on the rate tangent modulus method of Peirce *et al.* (1984).

3. NUMERICAL RESULTS

The impact loading on the specimen in Fig. 1 produces a compressive wave in the region between the two cracks. When the wave reaches the crack tip, the constraint induced by the remainder of the specimen induces rather large shear stresses, resulting in mode II type loading. Experiments carried out on a high-strength steel exhibited two distinct fracture modes (Kalthoff and Winkler, 1988; Kalthoff, 1988): at low loading rates there was a brittle cleavage mode of failure with crack growth occurring at slightly less than 70° from the initial crack plane (positive angles are counter clockwise from the y^1-axis in Fig. 1), while at sufficiently high loading rates shear localization following a path $\approx -10°$ from the initial crack plane occurred. Failure within the shear band was by ductile void growth and arrest was observed after a certain length, seen to be about 15 mm by Kalthoff (1988). By way of contrast, at low loading rates complete failure of the specimen took place. Thus, in the experiments of Kalthoff and Winkler (1988) on steel and also in those of Ravi-Chandar (1994) on polycarbonate, brittle behavior was observed at low loading rates and ductile behavior at high loading rates—exactly the opposite of the usual brittle–ductile transition.

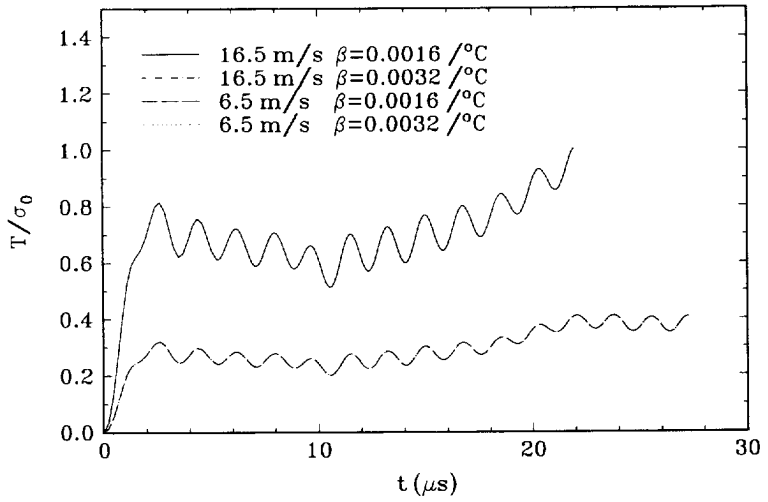

Fig. 4. Traction, force per unit initial area, at the impacted surface versus time. The traction is normalized by the reference strength σ_0. In all calculations here $\sigma_0 = 1000$ MPa.

Our calculations indicate that the observed behavior is mainly the outcome of a competition between thermal softening-induced localization and cleavage. Porosity-induced softening appears to play an important, but secondary, role. Here, in order to explore this competition, calculations are carried out for two values of the thermal softening coefficient, $\beta = 0.0016\,^{\circ}\mathrm{C}^{-1}$ and $\beta = 0.0032\,^{\circ}\mathrm{C}^{-1}$ in eqn (16) (see Fig. 2). Since thermo-mechanical properties are not given by Kalthoff and Winkler (1988) or Kalthoff (1988), a quantitative comparison with the experiments is not made.

The impact velocities considered are $V_1 = 6.5$ m s^{-1} and $V_1 = 16.5$ m s^{-1}, which correspond to projectile velocities of 13 and 33 m s^{-1}, respectively. The focus here is on the initiation of failure and the results presented pertain to a stationary crack unless specifically stated otherwise. Because adiabatic conditions are assumed, the porosity is uniformly distributed and the critical stress for cleavage is also spatially uniform, no material length scale enters the formulation. There is, however, a geometrical length that affects the stress and strain distributions near the crack tip—the crack tip radius. It is worth noting that Kalthoff and Winkler (1988) and Kalthoff (1990) reported that the projectile velocity at which the brittle–ductile transition occurred depended on the initial crack tip radius. Also, for a sufficiently blunt crack tip and with a sufficiently small impact velocity no damage was observed (Kalthoff and Winkler, 1988).

Figure 4 shows computed curves of traction versus end-displacement. The rise time of $t_r = 1.0$ μs in eqn (6) is evident in this figure and the oscillations are a consequence of the discretization. Over the time interval considered, the material essentially behaves in a linear elastic manner except near the crack tip. Hence, the traction versus time response in Fig. 4 is independent of the thermal softening characterization.

Curves of J, computed from eqn (18), versus time and crack tip opening, δ_t, versus time are shown in Fig. 5, where the current value of δ_t is measured at the nodal points at which the initial semi-circular crack tip is tangent to the flat crack faces. The evolutions of J and of δ_t are also independent of the thermal softening characterization over the time interval shown. The stress levels build up more quickly at higher impact velocities so that J increases more rapidly for $V_1 = 16.5$ m s^{-1} than for $V_1 = 6.5$ m s^{-1}. Due to the expansion of the material between the two cracks, the crack tip opening, δ_t, decreases as the stressing at the crack tip increases. For high enough impact velocities and small enough initial crack openings, contact of the opposite sides of the crack faces can occur. However, this was not observed in the computations reported here.

Contours of maximum principal stress, σ_1, and matrix effective plastic strain, $\bar{\varepsilon}$, are shown in Fig. 6 for the case with $V_1 = 16.5$ m s^{-1} and $\beta = 0.0032\,^{\circ}\mathrm{C}^{-1}$ at $t = 10.2$ μs. The maximum principal stress is negative toward the center of the specimen and positive above the initial crack line. Lee and Freund (1990) found that the maximum circumferential stress

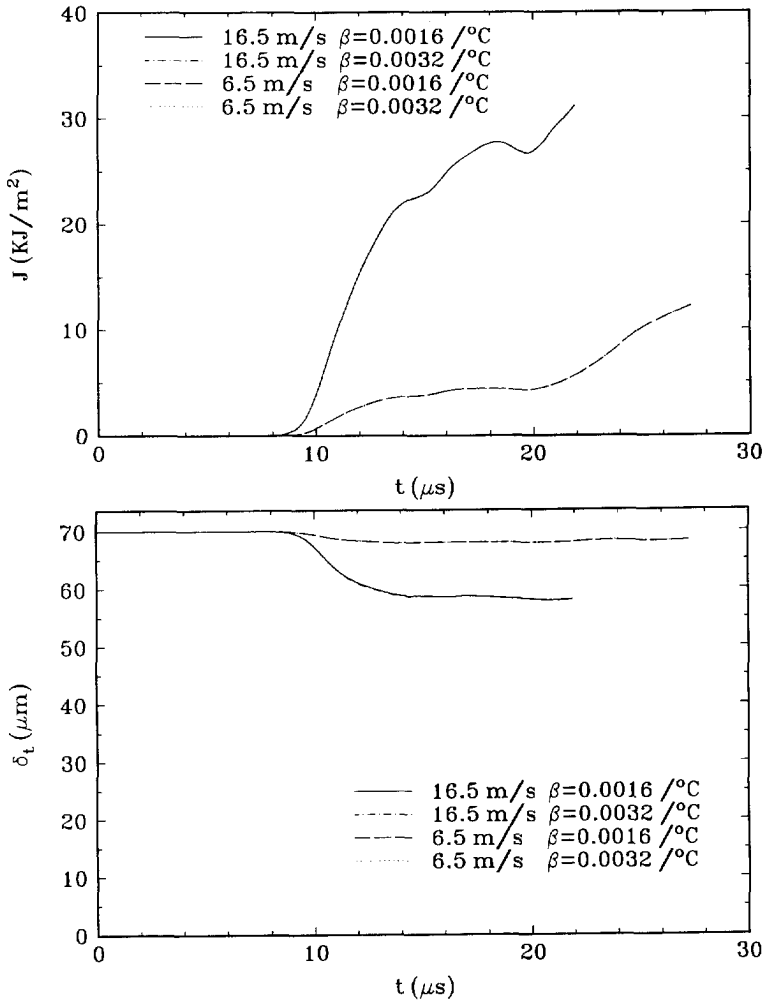

Fig. 5. (a) J versus time. J is defined by eqn (18) and includes both an area integral term and a contour integral term. (b) Crack tip opening, δ_t, versus time.

in the linear elastic asymptotic field occurred at about 63° from the crack line. There is a region near the crack tip in Fig. 6(a), exhibited by the $\sigma_1 = 600$ MPa contour, that is consistent with this. There are two bands of high straining in Fig. 6(b); directly ahead of the initial tip and at $\approx -135°$ from the initial crack plane. Note, however, that the stress state is compressive in the band at $\approx -135°$ from the initial crack plane. The highest tensile stressing in Fig. 6(a) occurs where the strains are very small and the material response is essentially elastic. At this early stage, the field distributions are nearly independent of the value of the thermal softening coefficient β and the qualitative features of the distribution pertain to both values of impact velocity.

Figure 7 shows curves of the maximum principal stress in the material, $\sigma_{1,\max}$, and the maximum value of the matrix plastic strain in the material, $\bar{\varepsilon}_{\max}$, versus time for all four computations. The mesh around the initial notch is not extremely fine so the specific values in Fig. 7 may change with increased mesh resolution, but the trends are expected to be the same. With $V_1 = 6.5$ m s^{-1}, there is very little dependence on the value of the thermal softening coefficient β, because the strains are not large enough for thermal softening to play a substantial role. On the other hand, with $V_1 = 16.5$ m s^{-1}, $\bar{\varepsilon}_{\max}$ is larger and $\sigma_{1,\max}$ is lower for the case with $\beta = 0.0032°\text{C}^{-1}$ than for the case with $\beta = 0.0016°\text{C}^{-1}$. The dip in $\sigma_{1,\max}$, with a corresponding plateau in plastic strain, at ≈ 18 μs is due to the arrival of an unloading wave. With $V_1 = 16.5$ m s^{-1} and $\beta = 0.0032°\text{C}^{-1}$ the value of $\sigma_{1,\max}$ is decreasing rather rapidly for $t > 20.4$ μs.

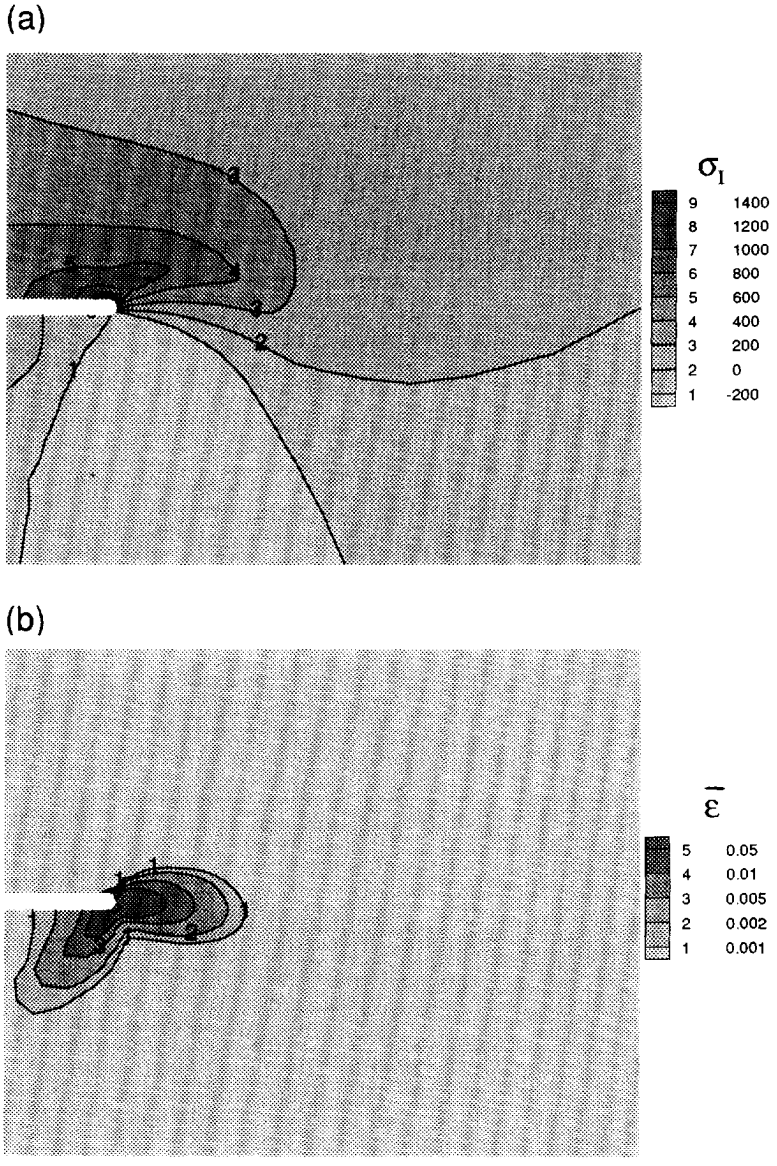

Fig. 6. Contours of (a) maximum principal stress, σ_I, and (b) matrix effective plastic strain, $\bar{\varepsilon}$, for $V_1 = 16.5$ m s^{-1} and $\beta = 0.0032$ C^{-1} at $t = 10.2$ μs.

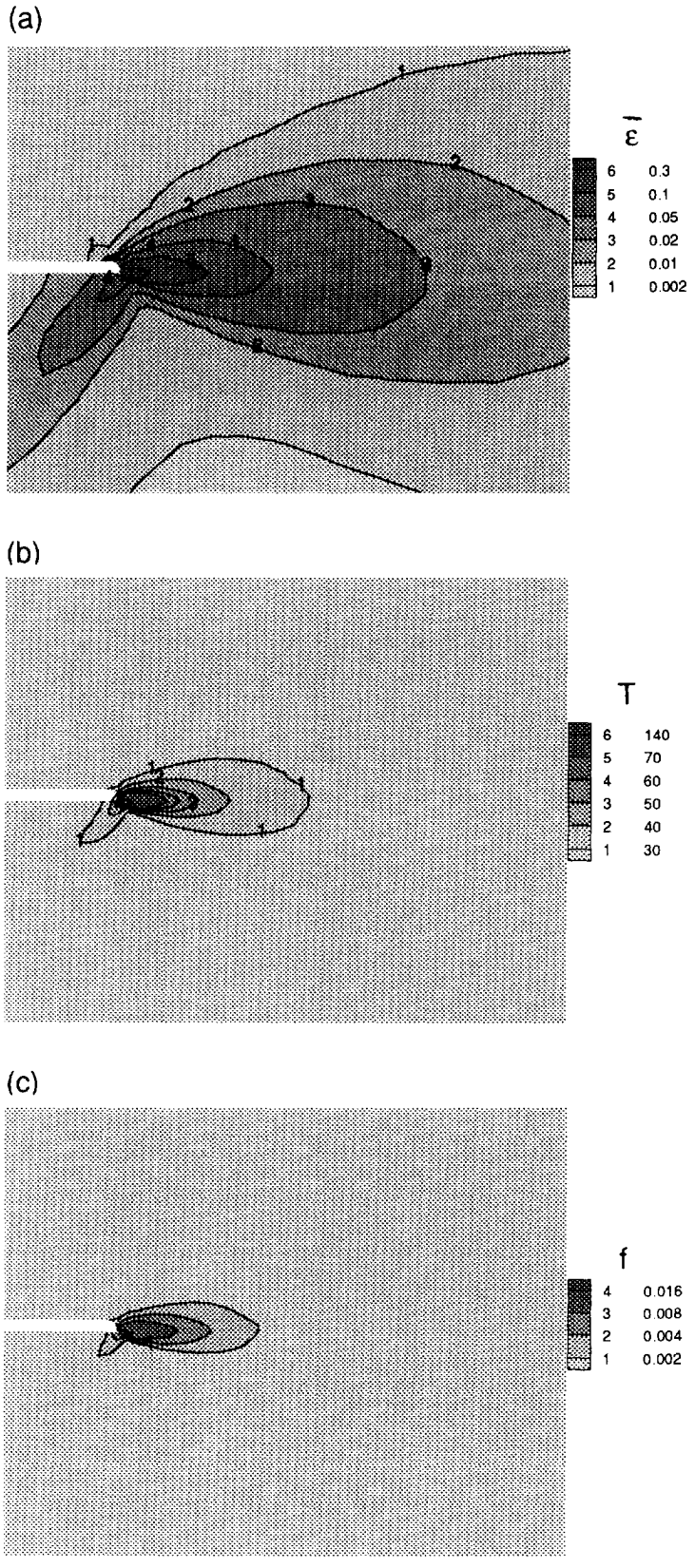

Fig. 9. Contours of various field quantities for $V_1 = 16.5$ m s^{-1} and $\beta = 0.0032$ C^{-1} at $t = 21.9$ μs. (a) Matrix plastic strain, $\bar{\varepsilon}$; (b) temperature, T; and (c) void volume fraction, f.

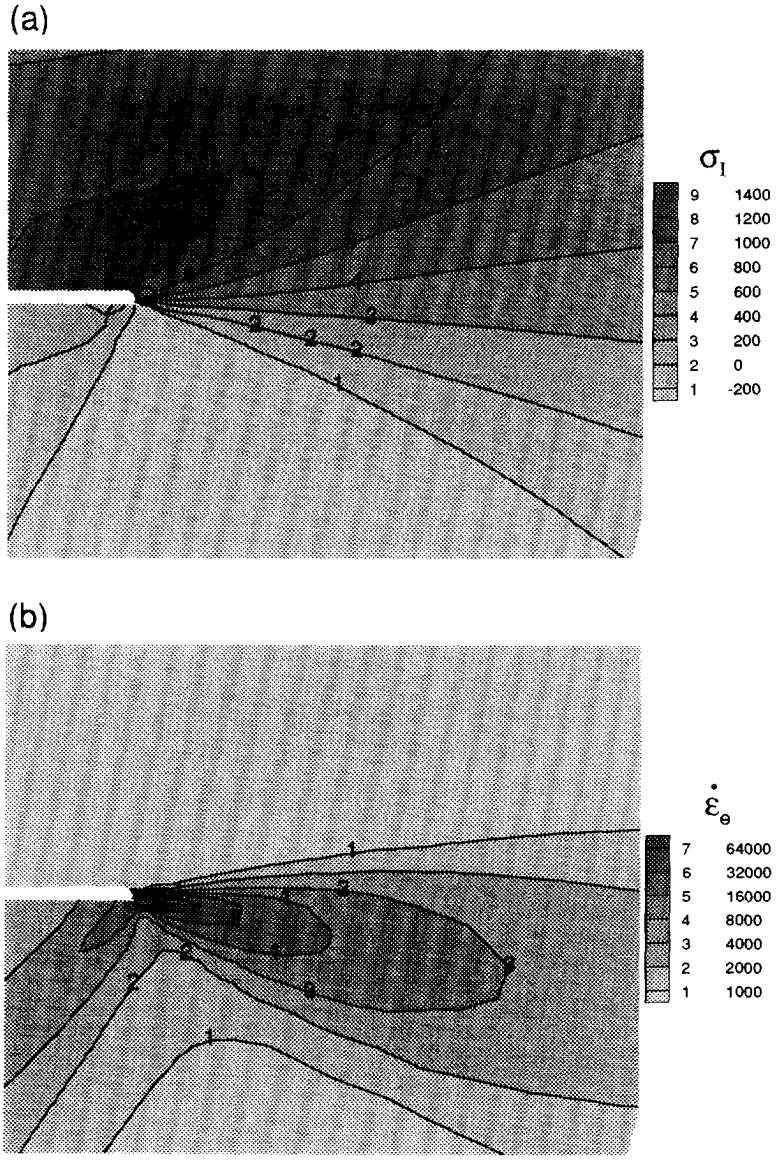

Fig. 10. Contours of (a) maximum principal stress, σ_1, and (b) effective strain rate, $\dot{\varepsilon}_e$, for $V_1 = 16.5$ m s^{-1} and $\beta = 0.0032\,^{\circ}$C^{-1} at $t = 21.9$ μs.

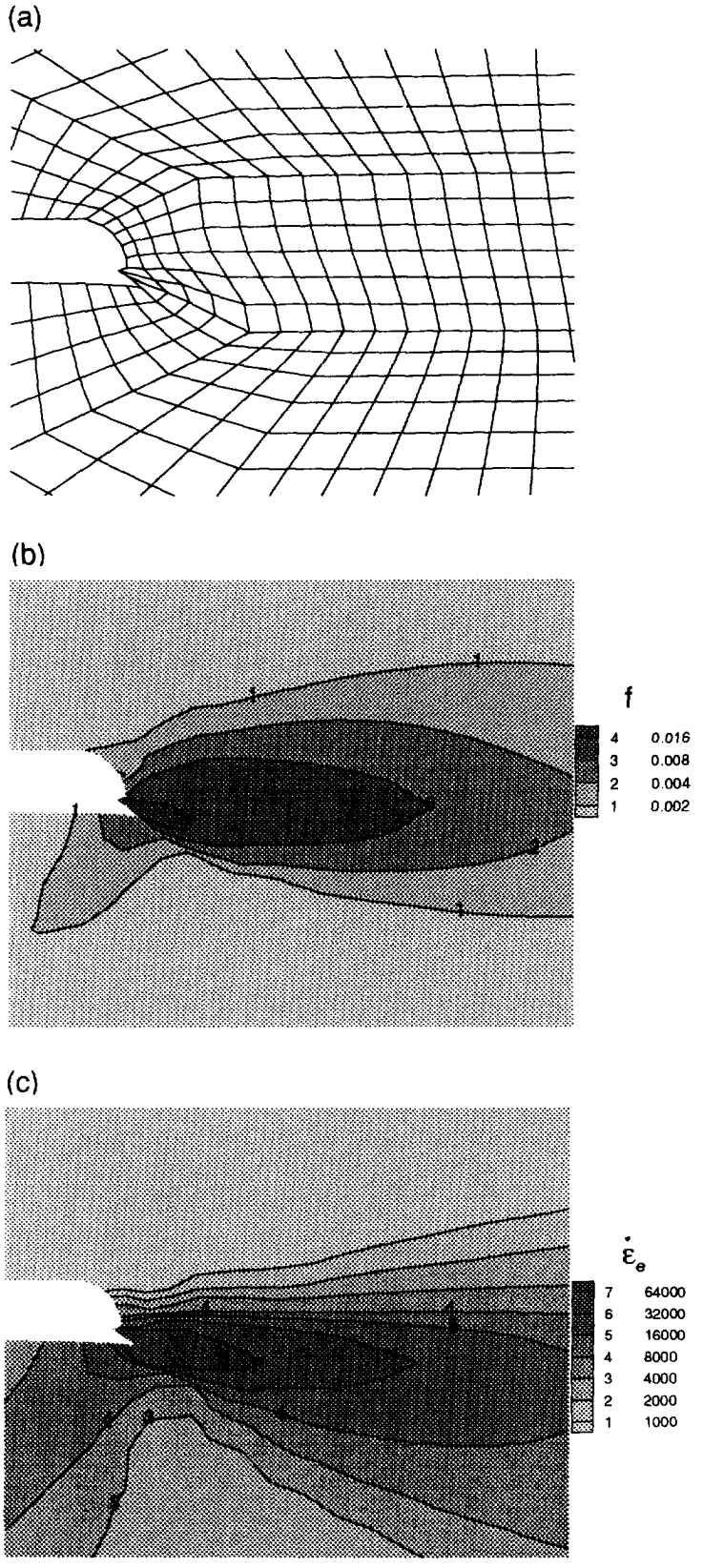

Fig. 11. Region near the crack tip for $V_1 = 16.5$ m s^{-1} and $\beta = 0.0032°C^{-1}$ at $t = 21.9$ μs. (a) Deformed finite element mesh; (b) contours of void volume fraction, f; and (c) effective strain rate, $\dot{\varepsilon}_e$.

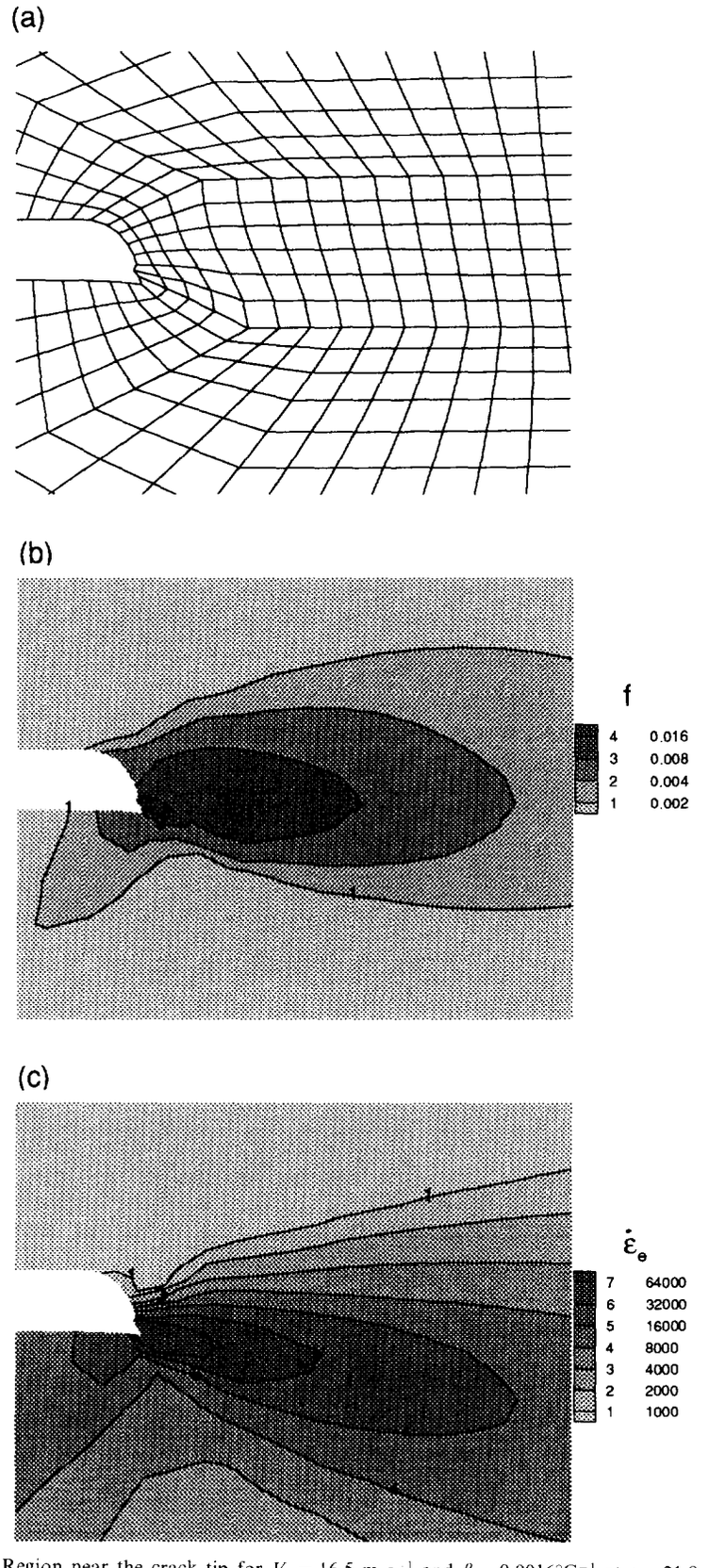

Fig. 12. Region near the crack tip for $V_1 = 16.5$ m s^{-1} and $\beta = 0.0016°C^{-1}$ at $t = 21.9$ μs. (a) Deformed finite element mesh; (b) contours of void volume fraction, f; and (c) effective strain rate, $\dot{\varepsilon}_e$.

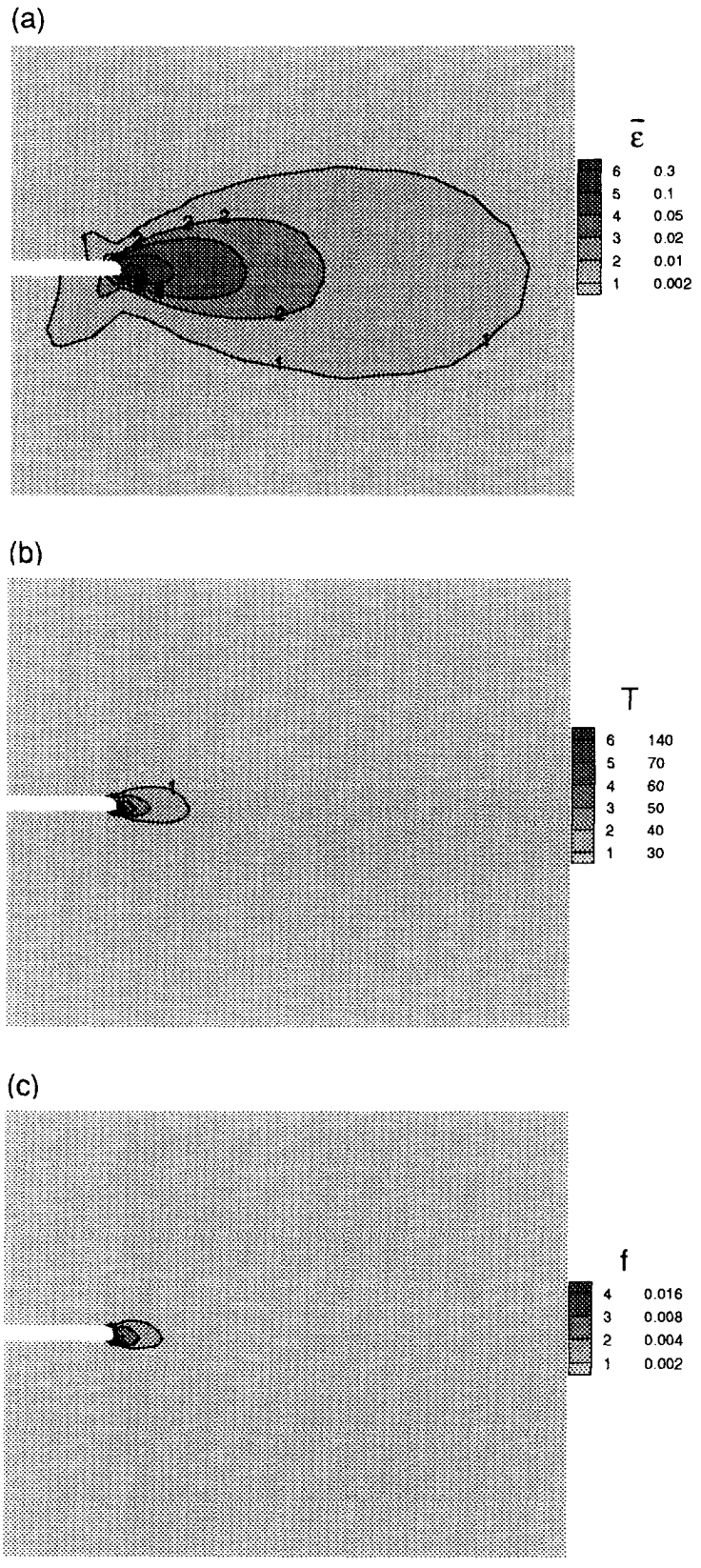

Fig. 13. Contours of various field quantities for $V_1 = 6.5\ \mathrm{m\ s^{-1}}$ and $\beta = 0.0032^{\circ}\mathrm{C}^{-1}$ at $t = 27.3\ \mu\mathrm{s}$. (a) Matrix plastic strain, $\bar{\varepsilon}$; (b) temperature, T; and (c) void volume fraction, f.

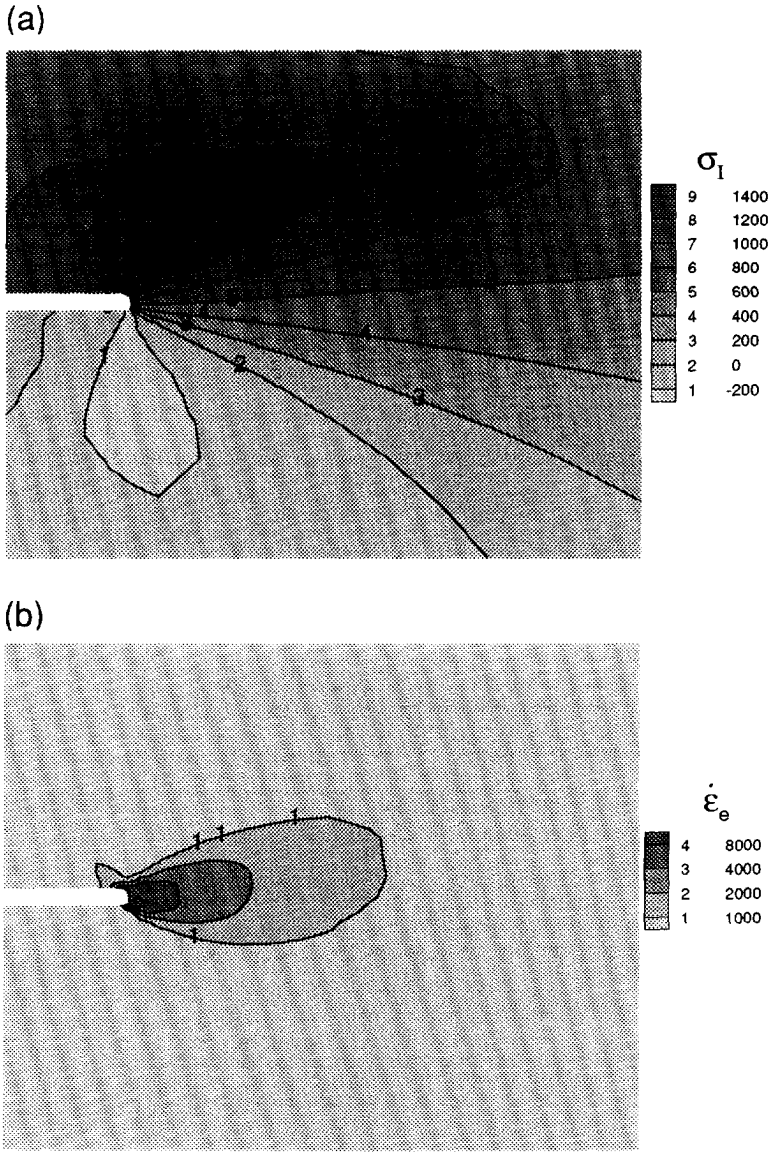

Fig. 14. Contours of (a) maximum principal stress, σ_I, and (b) effective strain rate, $\dot{\varepsilon}_e$, for $V_1 = 6.5$ m s^{-1} and $\beta = 0.0032$ C^{-1} at $t = 27.3$ μs.

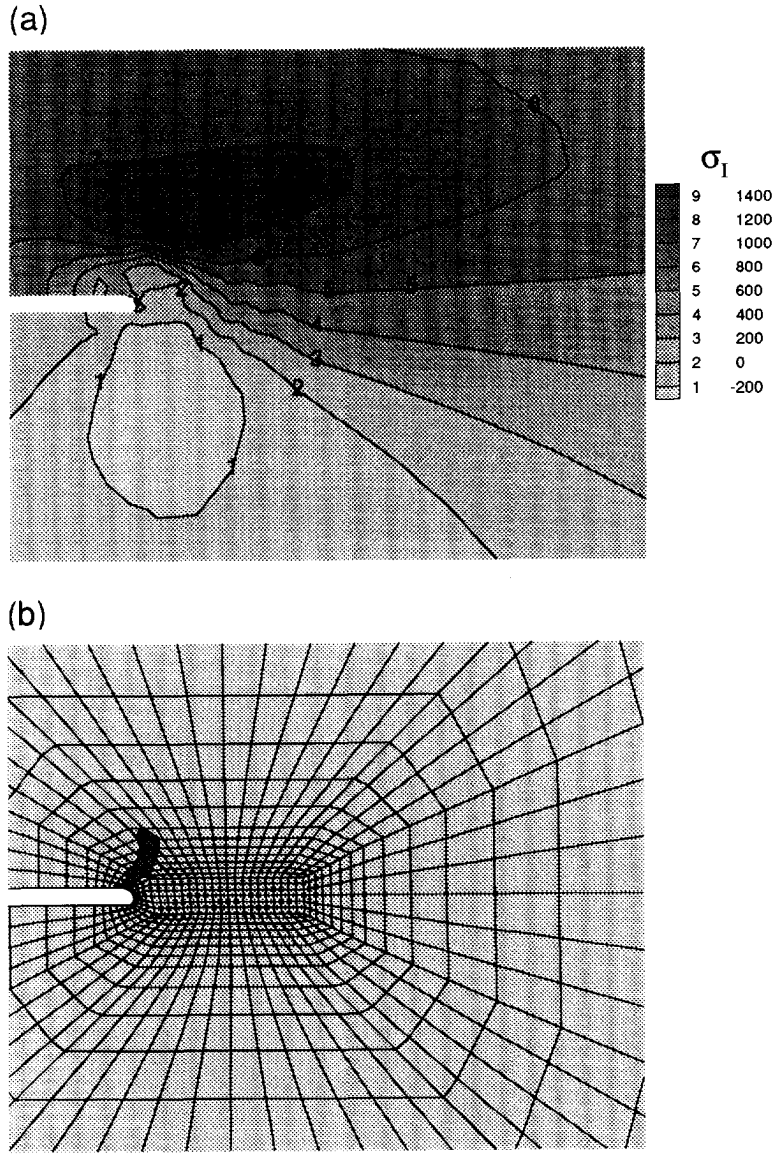

Fig. 15. (a) Contours of maximum principal stress, σ_I, and (b) deformed mesh with a contour showing which elements have cleaved for $V_1 = 6.5\ \mathrm{m\ s^{-1}}$, $\beta = 0.0032^{\circ}\mathrm{C}^{-1}$ and $\sigma_c = 1900$ MPa.

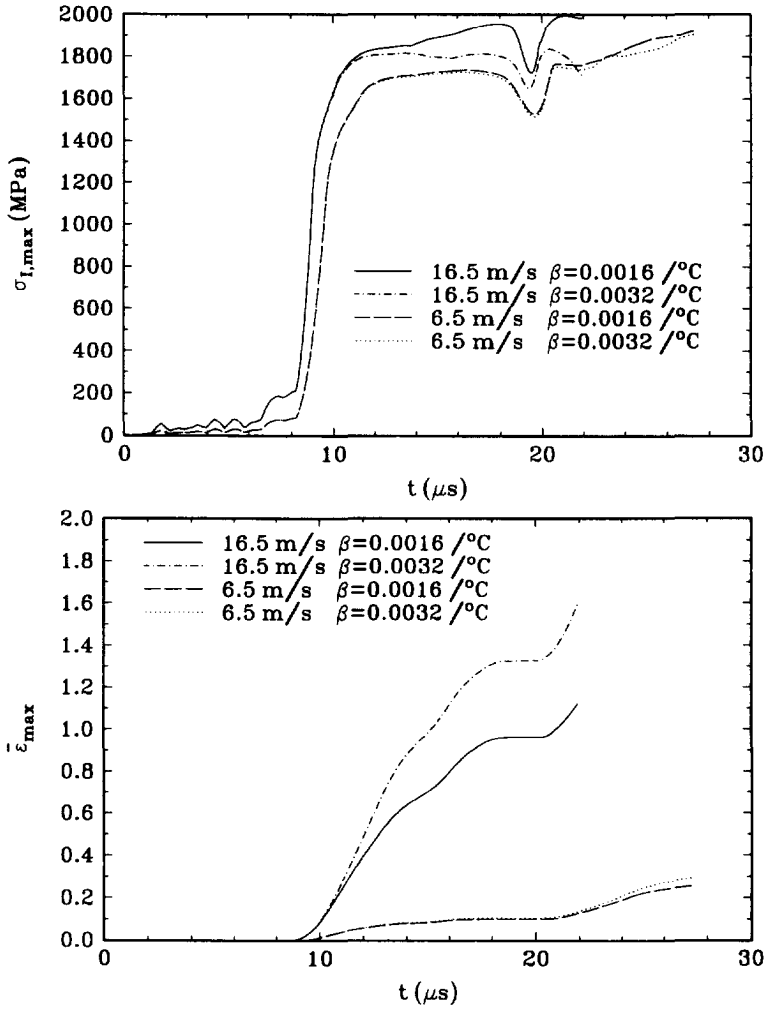

Fig. 7. Curves of (a) the largest value of the maximum principal stress in the material, $\sigma_{1,max}$, and (b) the largest value of the matrix plastic strain in the material, $\bar{\varepsilon}_{max}$, versus time.

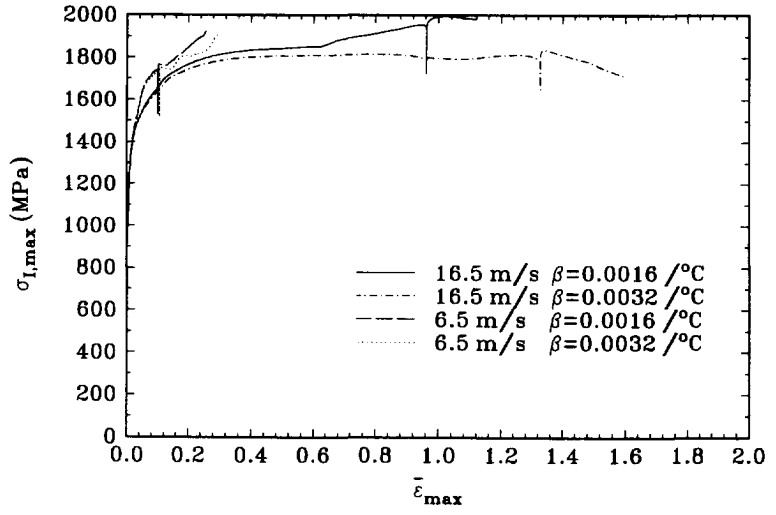

Fig. 8. Curves of the largest value of the maximum principal stress in the material, $\sigma_{1,max}$, versus the largest value of the matrix plastic strain in the material, $\bar{\varepsilon}_{max}$.

The maximum principal stress in the material, $\sigma_{1,\max}$, is plotted against the maximum plastic strain in the material, $\bar{\varepsilon}_{\max}$, in Fig. 8. The sharp drop seen in each case is due to the unloading wave. Here, it can be seen that the value of $\sigma_{1,\max}$ for a given value of $\bar{\varepsilon}_{\max}$ is greater with the lower impact velocity, $V_1 = 6.5$ m s^{-1}, than with the higher impact velocity, $V_1 = 16.5$ m s^{-1}. Also, at $V_1 = 16.5$ m s^{-1} a peak value of $\sigma_{1,\max} = 1837$ MPa is attained with $\beta = 0.0032^\circ\text{C}^{-1}$, while with $\beta = 0.0016^\circ\text{C}^{-1}$ $\sigma_{1,\max}$ reaches 2000 MPa (at the end of the time interval shown $\sigma_{1,\max}$ is not increasing, but a continuation of this computation showed that $\sigma_{1,\max}$ subsequently increased).

Figure 9 shows contours of matrix plastic strain, temperature and void volume fraction for the case with $V_1 = 16.5$ m s^{-1} and $\beta = 0.0032^\circ\text{C}^{-1}$ at $t = 21.9$ μs. This is the last stage of the computation for this case and thus is at a stage where $\sigma_{1,\max}$ is falling. The plastic strain contours in Fig. 9(a) show that the magnitude of the plastic strains in front of the crack tip are larger than at -135°. At the stage of deformation in Fig. 9, the temperature increase is not very large except in a few highly distorted elements right near the crack tip, and the void volume fraction is less than 0.06 throughout the specimen.

Contours of maximum principal stress, σ_1, and effective strain rate, $\dot{\varepsilon}_e$, are shown in Fig. 10. Here, $\dot{\varepsilon}_e$ is defined as

$$\dot{\varepsilon}_e = \sqrt{\left(\frac{2}{3}\mathbf{d}' : \mathbf{d}'\right)}, \tag{20}$$

where $\mathbf{d}'$ is the deviator of the rate of deformation. As in Fig. 6, the maximum principal stress is above the crack tip and is negative toward the central portion of the specimen. The high local strain rates together with the drop in σ_1 are indicative of the onset of the localization of deformation. In Fig. 10(b), the maximum plastic strain rate is focused in front of the crack tip, directed somewhat down toward the middle of the specimen, which is consistent with the direction of localization and ductile damage seen by Kalthoff (1988, 1990). The role of the porosity-induced softening seems to be to promote focusing of the highest strain rates ahead of the crack tip where σ_1 is positive, in preference to the -135° orientation where σ_1 is negative.

The region near the crack tip for this case is shown in Fig. 11. The very highly distorted elements at the crack tip can be seen in Fig. 11(a). The effective plastic strain, the temperature, the porosity and the effective strain rate all take on their largest values in these elements. The greater concentration of the strain rate ahead of the crack tip than at -135 is also evident in Fig. 11(c). Figure 12 shows the same region as Fig. 11, except that it pertains to the case with $V_1 = 16.5$ m s^{-1} and $\beta = 0.0016^\circ\text{C}^{-1}$. Here also, $t = 21.9$ μs. The strain rates are somewhat less localized than for the case with $\beta = 0.0032^\circ\text{C}^{-1}$. For example, the accumulated strain at the notch tip is smaller than in Fig. 11, as can be seen by comparing the deformed mesh plots in Figs 11(a) and 12(a). Although the qualitative features of the contours are the same as in Fig. 11, the key difference between these two calculations is that with $\beta = 0.0032^\circ\text{C}^{-1}$ the increased deformation rate has led to a relaxation of the maximum tensile stress, whereas with $\beta = 0.0016^\circ\text{C}^{-1}$ no such relaxation has occurred.

Figure 13 shows contours of matrix plastic strain, temperature and void volume fraction for the case with $V_1 = 6.5$ m s^{-1} and $\beta = 0.0032^\circ\text{C}^{-1}$ at $t = 27.3$ μs. The reduced strain concentration ahead of the crack tip, and particularly at -135°, can be seen in Fig. 13(a). Figure 14 shows contours of maximum principal stress and effective strain rate for the same case as in Fig. 13. Note that the peak strain rate contour shown in Fig. 14 is a factor of eight smaller than the peak strain rate contour in Fig. 10. Also, note that while the strain rate is also focused in front of the crack tip, the contours are quite differently shaped from those in Fig. 11(b) and are directed away from the center of the specimen.

Figure 15 shows results from a computation with some cleavage crack growth. Here, $V_1 = 6.5$ m s^{-1} and $\beta = 0.0032^\circ\text{C}^{-1}$ and the critical stress for cleavage was taken to be $\sigma_c = 1900$ MPa. The maximum principal stress is in front of the current crack tip. The stress redistribution accompanying cleavage can be seen by comparing Figs 15(a) and 14(a).

The darkened region in Fig. 15(b) shows the elements in which cleavage has occurred and the angle of growth is $\approx 65^{\circ}$. The focus here is on failure initiation and this calculation is only intended to give an indication of the initial direction of cleavage cracking. The cleavage criterion used does not contain a material length scale so that the crack speed in Fig. 15 is mesh dependent. A more complete investigation of cleavage crack growth could be based on the formulation in Tvergaard and Needleman (1993), which does incorporate a material length scale. Such an investigation would also require a fine mesh along the cleavage crack growth path.

4. DISCUSSION

The elastic–viscoplastic constitutive relation accounting for both ductile failure by void growth to coalescence and brittle failure by cleavage in body-centered cubic metals has been used by Tvergaard and Needleman (1986, 1988) to analyze the ductile–brittle transition for Charpy V-notch specimens, and the same material model with the effect of adiabatic heating due to plastic dissipation incorporated has been used to study the brittle–ductile transition in dynamic crack growth (Tvergaard and Needleman, 1993) and in a three-dimensional analysis of the Charpy impact test (Mathur *et al.*, 1994). Typically, there is a transition range, in which more rapid loading gives rise to more brittle behavior. Experiments using the double edge-cracked specimen developed by Kalthoff (1988) to study crack growth under rapid shear loading have also shown a transition, but in the opposite sense so that higher loading rates tend to promote ductile behavior, and the question of main interest in the present paper is whether or not the material model is able to explain this opposite behavior.

Already at an early stage (Fig. 6) the computed near tip fields show higher tensile stress levels on one side of the crack tip, where brittle cracks were observed in the experiments, and higher strain levels ahead of the crack, where ductile crack growth was observed. Both tendencies continue to develop (Figs 9 and 10), and if the critical stress for cleavage failure is reached, the model leads to the prediction of brittle crack growth at an angle of about 65° from the initial crack plane (Fig. 15). So the question is, why would this critical stress level be reached for a low loading rate and not for a high rate? The computations show a case for a particular set of material parameters (Fig. 7), where at a high loading rate the maximum principal tensile stress reaches a peak value and then decays rapidly, whereas at a lower loading rate the stress value keeps increasing above this peak value. In this case the type of brittle–ductile transition observed in the experiments (Kalthoff and Winkler, 1988; Kalthoff, 1988) is directly predicted by the present computations. In the case of high rate loading, where brittle failure is not predicted, the thermal softening combined with void growth softening in front of the crack tip will eventually lead to localized shear failure in a thin layer of material ahead of the tip, corresponding to the mode of ductile crack growth observed in the experiments. The experiments of Ravi-Chandar (1994) on polycarbonate suggest that this sort of opposite fracture mode transition under mode II type loading conditions may occur quite generally when there is a competition between a strain-driven ductile failure mode and a stress-driven brittle failure mode.

The strain rates in the highly strained region in front of the crack tip are so high, both in the case of a high loading rate (Fig. 10) and in the case of a lower rate (Fig. 11), that the assumption of adiabatic heating is very realistic. Thus, the possibility of a stronger effect of heat conduction at a lower loading rate cannot explain a reduced tendency for thermally-induced localization. Heat conduction, however, may play a more significant role in affecting the propagation of the shear band and the development of the ductile failure mode. On the other hand, the high tensile stresses occur on the side of the crack tip opposite to the side loaded by the projectile, and this development must be shielded by the growth of the softening region in front of the tip, between the primary stress wave and the point where the tensile stress peak develops. At the higher rate of loading this softening region grows more rapidly, so that the tensile stress peak has less time to develop (by stress waves), before thermal softening starts to dominate. Thus, it appears that the speed of loading, determining the rate of build up of the thermal softening region, compared with the wave

speed may be an important parameter in the brittle–ductile transition found in the specimen analyzed here.

Acknowledgements—The support of the Office of Naval Research through grant N00014-89-J-3054 is gratefully acknowledged. The computations reported on here were carried out on the Cray C90 at the Pittsburgh Supercomputer Center.

REFERENCES

Belytschko, T., Chiapetta, R.L. and Bartel, H.D. (1976). Efficient large scale non-linear transient analysis by finite elements. *Int. J. Numer. Meth. Engng* **10,** 579–596.

Chu, C.C. and Needleman, A. (1980). Void nucleation effects in biaxially stretched sheets. *J. Engng Mater. Tech.* **102,** 249–256.

Finot, M., Shen, Y.-L., Needleman, A. and Suresh, S. (1994). Micromechanical modelling of reinforcement fracture in particle-reinforced metal–matrix composites. *Metall. Mater. Trans.* **25A,** 2403–2420.

Gurson, A.L. (1975). Plastic flow and fracture behavior of ductile materials incorporating void nucleation, growth and interaction. Ph.D. Thesis, Brown University.

Kalthoff, J.K. (1988). Shadow optical analysis of dynamic shear fracture. *Opt. Engng* **27,** 127–133.

Kalthoff, J.K. (1990). Transition in the failure behavior of dynamically shear loaded cracks. In *Proceedings of the 11th U.S. National Congress. Appl. Mech., Appl. Mech. Rev.* **43,** S247–S250.

Kalthoff, J.K. and Winkler, S. (1988). Failure mode transition at high rates of loading. In *Proceedings of the International Conference on Impact Loading and Dynamic Behaviour of Materials* (Edited by C.Y. Chiem, H.D. Kunze and L.W. Meyer), pp. 43–56. Deutsche Gesellshaft für Metallkunde.

Krieg, R.D. and Key, S.W. (1973). Transient shell response by numerical time integration. *Int. J. Numer. Meth. Engng* **7,** 273–286.

Lee, Y.J. and Freund, L.B. (1990). Fracture initiation due to asymmetric impact loading of an edge cracked plate. *J. Appl. Mech.* **57,** 104–111.

Mason, J.J., Rosakis, A.J. and Ravichandran, G. (1994). Full field measurements of the dynamic deformation field around a growing adiabatic shear band at the tip of a dynamically loaded crack or notch. *J. Mech. Phys. Solids* **42,** 1679–1697.

Mathur, K.K., Needleman, A. and Tvergaard, V. (1994). 3D analysis of failure modes in the Charpy impact test. *Modelling Simul. Mater. Sci. Engng* **2,** 617–635.

Moran, B. and Shih, C.F. (1987a). Crack tip and associated domain integrals from momentum and energy balance. *Engng Fracture Mech.* **27,** 615–642.

Moran, B. and Shih, C.F. (1987b). A general treatment of crack tip contour integrals. *Int. J. Fracture* **35,** 295–310.

Mudry, F. (1987). A local approach to cleavage fracture. *Nucl. Engng Design* **105,** 65–76.

Needleman, A. and Tvergaard, V. (1991a). An analysis of dynamic, ductile crack growth in a double edge cracked specimen. *Int. J. Fracture* **49,** 41–67.

Needleman, A. and Tvergaard, V. (1991b). A numerical study of void disribution effects on dynamic, ductile crack growth. *Engng Fracture Mech.* **38,** 157–173.

Needleman, A. and Tvergaard, V. (1994). Mesh effects in the analysis of dynamic ductile crack growth. *Engng Fracture Mech.* **47,** 75–91.

Peirce, D., Shih, C.F. and Needleman, A. (1984). A tangent modulus method for rate dependent solids. *Comput. Struct.* **18,** 875–887.

Prakash, V. and Clifton, R.J. (1992). Experimental and analytical investigation of dynamic fracture under conditions of plane strain. *Proceedings of the 22nd National Symposium Fracture Mechanics ASTM STP* **1131,** 412–444.

Ravi-Chandar, K. (1994). Dynamic fracture under shear loading. *Int. J. Solids Structures.* In press.

Rice, J.R. (1968). A path independent integral and the approximate analysis of strain concentration by notches and cracks. *J. Appl. Mech.* **35,** 379–386.

Ritchie, R.O., Knott, J.F. and Rice, J.R. (1973). On the relationship between critical tensile stress and fracture toughness in mild steel. *J. Mech. Phys. Solids* **21,** 395–410.

Taylor, G.I. and Quinney, H. (1934). The latent energy remaining in a metal after cold working. *Proc. R. Soc.* **A143,** 307–326.

Tvergaard, V. (1981). Influence of voids on shear band instabilities under plane strain conditions. *Int. J. Fracture* **17,** 389–407.

Tvergaard, V. (1982). On localization in ductile materials containing spherical voids. *Int. J. Fracture* **18,** 237–252.

Tvergaard, V. and Needleman, A. (1984). Analysis of the cup-cone fracture in a round tensile bar. *Acta Metall.* **32,** 157–169.

Tvergaard, V. and Needleman, A. (1986). Effect of material rate sensitivity on failure modes in the Charpy V-notch test. *J. Mech. Phys. Solids* **34,** 213–241.

Tvergaard, V. and Needleman, A. (1988). An analysis of temperature and rate dependence of charpy V-notch energies for a high nitrogen steel. *Int. J. Fracture* **37,** 197–215.

Tvergaard, V. and Needleman, A. (1992). Effect of crack meandering on dynamic, ductile fracture. *J. Mech. Phys. Solids* **40,** 447–471.

Tvergaard, V. and Needleman, A. (1993). An analysis of the brittle–ductile transition in dynamic crack growth. *Int. J. Fracture* **59,** 53–67.

Zhou, M., Rosakis, A.J. and Ravichandran, G. (1994). Dynamically propagating shear bands in prenotched plates. GALCIT Report SM94-1, Caltech, Pasadena, California.